

## Fe solubility, growth mechanism, and luminescence of Fe doped ZnO nanowires and nanorods grown by evaporation-deposition

Belén Alemán, Yanicet Ortega, José Ángel García, Paloma Fernández, and Javier Piqueras

Citation: *J. Appl. Phys.* **110**, 014317 (2011); doi: 10.1063/1.3609073

View online: <http://dx.doi.org/10.1063/1.3609073>

View Table of Contents: <http://jap.aip.org/resource/1/JAPIAU/v110/i1>

Published by the AIP Publishing LLC.

---

### Additional information on J. Appl. Phys.

Journal Homepage: <http://jap.aip.org/>

Journal Information: [http://jap.aip.org/about/about\\_the\\_journal](http://jap.aip.org/about/about_the_journal)

Top downloads: [http://jap.aip.org/features/most\\_downloaded](http://jap.aip.org/features/most_downloaded)

Information for Authors: <http://jap.aip.org/authors>



# Fe solubility, growth mechanism, and luminescence of Fe doped ZnO nanowires and nanorods grown by evaporation-deposition

Belén Alemán,<sup>1,a)</sup> Yanicet Ortega,<sup>1</sup> José Ángel García,<sup>2</sup> Paloma Fernández,<sup>1</sup> and Javier Piqueras<sup>1</sup>

<sup>1</sup>Dpt. Física de Materiales, Facultad de Ciencias Físicas, Universidad Complutense de Madrid, 28040 Madrid, Spain

<sup>2</sup>Departamento de Física Aplicada II, Apartado 644 Universidad del País Vasco, 48080, Spain

(Received 12 April 2011; accepted 7 June 2011; published online 15 July 2011)

Fe doped ZnO nanowires, nanorods, and urchin-like nanostructures have been grown using an evaporation-deposition method with compacted mixtures of ZnS and Fe<sub>2</sub>O<sub>3</sub> powders, with different Fe contents as precursors. Treatments at 950 °C under argon flow lead to the growth of iron doped nanowires, nanorods, and other nanostructures on the surface of the compacted sample. The incorporation of iron into the nanostructures has been investigated via energy dispersive spectroscopy as well as by cathodoluminescence in a scanning electron microscope and photoluminescence in an optical microscope. The iron content in the structures is limited to the range of 0.5–0.7 at.% and does not depend on the content in the precursor. Bright and dark field imaging and twist contour analysis via transmission electron microscopy support the possibility of a dislocation driven growth of the nanowires. © 2011 American Institute of Physics. [doi:10.1063/1.3609073]

## I. INTRODUCTION

The doping of one-dimensional semiconductor nanostructures aimed at improving their electronic and optical properties is a field of present interest related to potential applications in nanotechnology. Due to the variety of ZnO applications, ZnO nanowires and other elongated nanostructures have been doped with different rare earth and metal ions, including different transition metal elements. In particular, Fe doped ZnO nanobelts,<sup>1</sup> nanorods,<sup>2,3</sup> nanocantilever arrays,<sup>4</sup> and nanowires<sup>5</sup> have been reported, and the influence of the dopant on the luminescence of nanostructured ZnO has been studied. It was found in Ref. 2 that Fe doping improves the optical properties of ZnO nanorods prepared via hydrothermal methods by causing a relative increase of the near band edge ultraviolet photoluminescence (PL) as compared with the deep level emission, usually referred to as green or green-yellow emission. In Ref. 4, the green PL emission of Fe doped ZnO nanocantilever arrays is reported to be strongly quenched, and Oh *et al.*<sup>3</sup> reported that Fe doped ZnO nanorods fabricated via a sonochemical route show enhanced deep level PL intensity. These results indicate that the influence of Fe atoms on the ZnO defect luminescence band in the nanostructures does not always have the same effect and could depend on the particular defect structure of the sample, which is normally related to the growth process used. In addition, the intra-ionic transitions of Fe can be observed in the luminescence spectra, as in the case of iron implanted ZnO nanowires.<sup>5</sup> In the present work, Fe doped ZnO nanowires, nanorods, and other nanostructures have been grown via a thermal evaporation-deposition method, and their luminescence properties have been investigated via cathodoluminescence (CL) in a scanning electron

microscope (SEM) and with micro-photoluminescence ( $\mu$ -PL) in an optical microscope as a function of the morphology and iron incorporation. The nanostructures were also characterized via x-ray diffraction (XRD), SEM, transmission electron microscopy (TEM and HRTEM), and energy dispersive x-ray spectroscopy (EDS).

## II. EXPERIMENTAL SECTION

ZnS and Fe<sub>2</sub>O<sub>3</sub> powders with purities of 99.999% and 99.98%, respectively, were used as precursors. Mixtures of the powders with 0.6, 3, and 5.8 at.% of Fe were prepared by milling the corresponding powders in a centrifugal ball mill. The mixture was then compacted to form disk-shaped samples about 7 mm in diameter and 2 mm in thickness. The samples were annealed under argon flow at 950 °C for 10 h. During annealing, ZnS decomposes and, as the furnace is not sealed for high vacuum conditions, slow oxidation takes place, and doped ZnO nanostructures grow on the disk surface via a catalyst free process. The samples obtained from precursors containing 0.6, 3, and 5.8 at.% Fe are hereinafter labeled as samples A, B, and C, respectively. The structure of the treated samples was investigated via XRD using an XPert Pro diffractometer. The morphology of the structures was characterized via SEM using a Leica 440, a Hitachi S2500, and a Fei Inspect SEM. EDS microanalysis was performed using a Leica 440 SEM with a Bruker AXS Quantax system. The luminescence measurements were performed with a CL system in a SEM working at 15–20 keV and 1–5 nA or with a  $\mu$ -PL system included in an Olympus optical microscope with the 365 nm (3.39 eV) or 435 nm (2.85 eV) emission lines of a Hg lamp and a Jobin Yvon Horiba SPEX 750 M monochromator.

For TEM measurements, samples were prepared by removing a bundle of nanostructures from the pellet surface and dispersing them in high-purity butanol. The

<sup>a)</sup>Author to whom correspondence should be addressed. Electronic mail: balemanl@fis.ucm.es.

nanostructure/butanol dispersion was ultrasonicated for 15 to 20 min. A few drops of the dispersion were then deposited on a TEM copper grid coated with a holey carbon film. The nanostructures were investigated via TEM bright field (BF) and dark field (DF) and with selected-area electron diffraction (SAED) in a Jeol Jem 3000 F transmission electron microscope operating at 300 kV.

### III. RESULTS AND DISCUSSION

The grazing incidence XRD pattern of sample B after thermal treatment (Fig. 1) represents the structure of all annealed samples, which corresponds to the hexagonal ZnO phase. SEM images show that the surface of all treated samples is covered by a dense distribution of nanowires and rods (Fig. 2(a)). In some places on the sample surfaces, the nanorods form urchin-like structures (Fig. 2(b)) in which the base of each rod is a hexagonal truncated pyramid (Fig. 2(c)). Figures 2(d) and 2(e) show the other nanostructures present in samples B and C, prepared with 3 and 5.8 at.% Fe in the precursor, respectively. In some areas of the samples, the wires appear to be intermixed with film or sheet-like structures that connect some of the wires and which can form incipient microtubes, as Figs. 2(d) and 2(e) show. Some of the SEM images suggest that the sheet structures are generated by the lateral growth of the nanowires (Fig. 2(f)). The morphology of the urchin structures is similar for all of the samples and does not depend appreciably on the Fe content in the precursor. Similar urchin structures have been observed in ZnO samples prepared with the same thermal method used here but with pure ZnS as a precursor,<sup>6</sup> but the complex morphology shown in Figs. 2(d) and 2(e) seems to be characteristic of the presence of the dopant.

EDS in the SEM does not show significant variations of the Fe content in the structures prepared with different amounts of Fe in the precursor mixture. In sample A, spectra recorded on a large area covered with nanowires show a well resolved Fe peak, and the estimated content of Fe is about 0.6 at.%. However, because part of the iron signal could arise from the disk surface beneath the wires, spectra were also

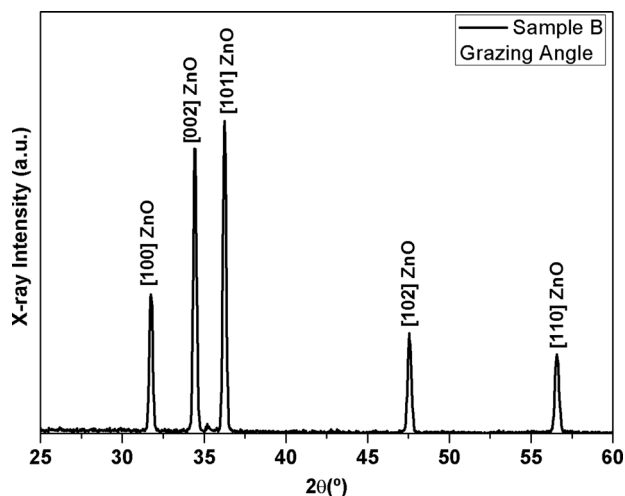


FIG. 1. XRD pattern of thermal treated sample B in which only ZnO peaks are observed.

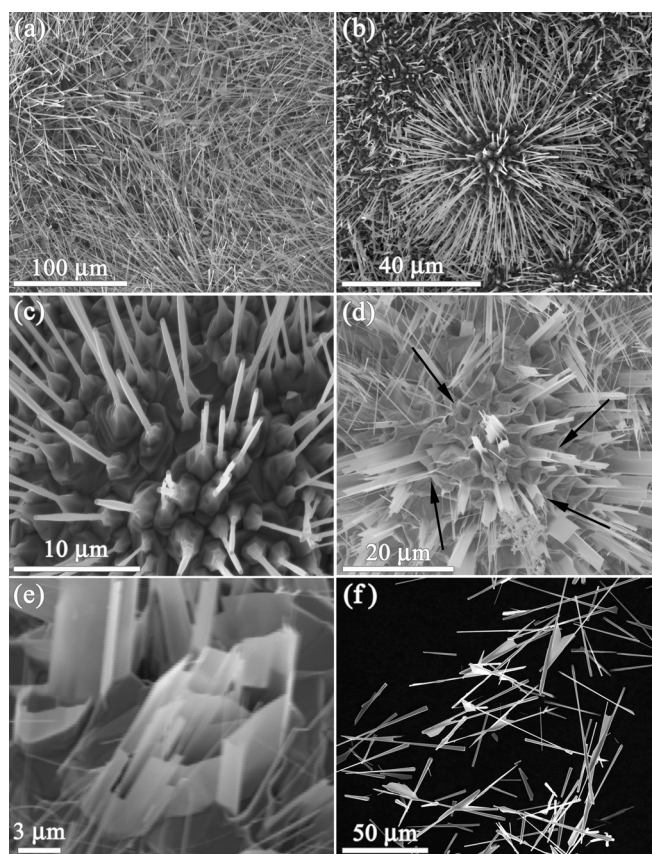


FIG. 2. SEM images of samples A, B, and C. (a) Nanowires, nanorods, and (b),(c) urchin-like structures. In samples B and C, with higher Fe contents, (d),(e) incipient microtubes and (f) nanowires connected by sheet-like structures are present.

recorded in isolated single wires. In this case the signal seems to be around the detection limit of the technique, and no well-resolved Fe peak was observed. EDS measurements performed directly on single rods, or on rods in the urchins, of sample B (Fig. 3) show Fe contents in the range of 0.5–0.7 at.%. Also, in sample C, with 5.8 at.% Fe in the precursor, the amount of Fe in the structures, as in those shown in Fig. 2(e), was found to be about 0.7 at.%. These results regarding the Fe content are subject to the error of the technique for low at.% analysis, so that the values have to be considered as approximate, and they indicate that in all samples the Fe at.% is in the range of 0.5–0.7. The Fe incorporation appears to be limited to this range independent of the amount of iron in the precursor powder mixture and of the final morphology of the nano- and microstructures. This result agrees with previous reports regarding Fe doping and solubility in ZnO crystals and nanostructures. Köster-Scherger *et al.*<sup>7</sup> have studied, via TEM, Fe doped ZnO crystals with inversion domains, and they concluded from electron energy loss spectroscopy measurements that the solid solubility of  $\text{Fe}^{3+}$  in defect free crystal regions is about 0.4 at.%, whereas in the inverted domains the  $\text{Fe}^{3+}$  concentration is depleted. In ZnO doped nanobelts,<sup>1</sup> the iron content measured via EDS was 1.58 at.%, but the authors considered that, due to the error in the analysis, the measurement served only as evidence of the presence of Fe in the sample. In Ref. 3, Fe doped ZnO nanorods fabricated via a sonochemical route contained about 0.9



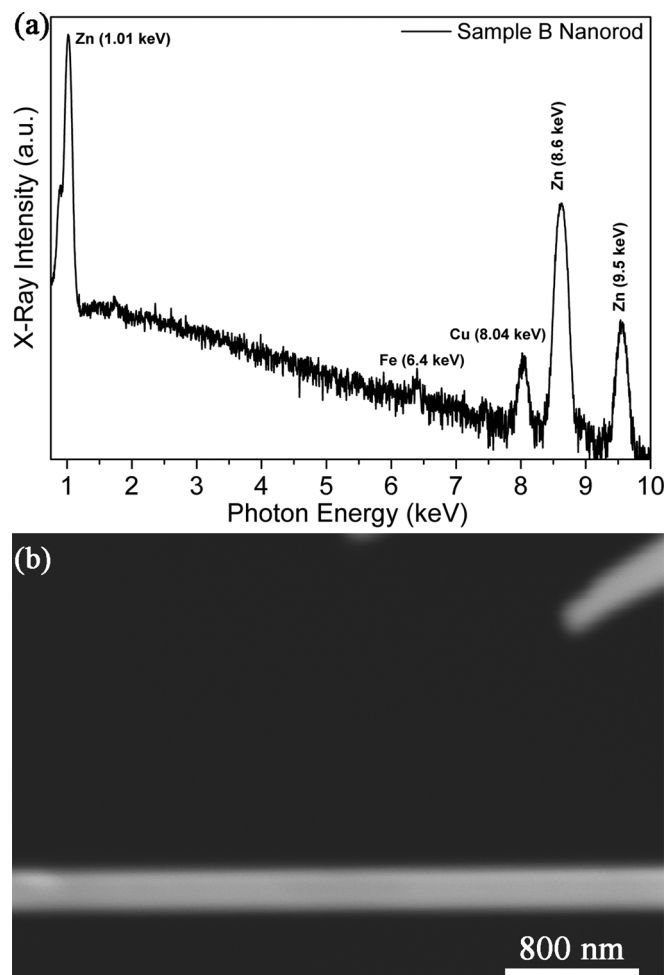


FIG. 3. (a) An EDS spectrum of a nanorod of sample B and (b) a SEM image of the nanorod. A small amount of Fe is detected. The Cu contribution is due to the sample holder.

at.% of dopant ions. The composition was measured using inductively coupled plasma atomic emission spectroscopy. A similar value of iron content (0.6 to 1 at.%), measured using EDS, was reported for Fe and Co codoped ZnO nanorods prepared via chemical vapor deposition.<sup>8</sup> On the other hand, the Fe content of ZnO nanocantilever arrays<sup>4</sup> was estimated by x-ray photoelectron spectroscopy (XPS) to be about 3 at.%, but because XPS is a surface technique, this figure cannot be directly compared with EDS data. These results, obtained using different characterization techniques and corresponding to Fe doped ZnO structures grown via different methods, show that the solubility of iron is likely in the range of 0.4–1 at.%, which agrees with the values obtained in the present work. The low solubility of Fe in ZnO has been previously reported for epitaxial films<sup>9</sup> and might be related to the stable trivalent state of iron in ZnO, whereas a higher solubility would be favored by a divalent state.

EDS measurements on a single nanowire in TEM agree with the above-described EDS results obtained in the SEM study. In the nanowires, as in those shown in Fig. 4, the Fe content was about 0.5 at. %.

HRTEM shows that the growth direction of the nanowires is [0001] (Fig. 4(a)). BF-TEM images also show the presence of dark fringes, or contours, perpendicular to the

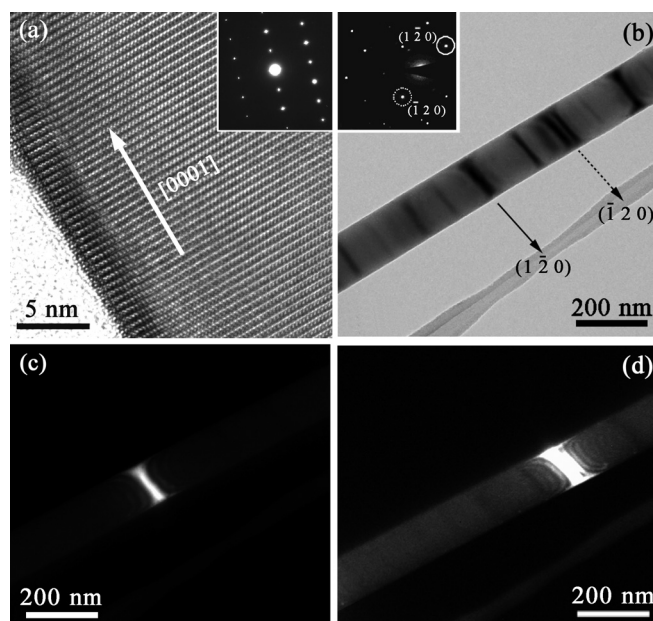


FIG. 4. (a) A HRTEM image of a ZnO:Fe nanowire showing the growth direction. The monocrystallinity of the nanowire is observed in the SAED in the inset. (b) BF-TEM image of the nanowire exhibiting contours along the growth direction. In the SAED in the inset, the  $(1\bar{2}0)$  (solid line) and  $(120)$  (dotted line) contours are pointed out. (c),(d) DF-TEM images of the nanowire taken with the  $(1\bar{2}0)$  and  $(120)$  spots, respectively.

growth axis (Fig. 4(b)), which moves along the axis upon slight tilting of the nanowire. In the frame of several recent reports on the screw dislocation driven growth of nanowires,<sup>10–13</sup> the possibility that these dark contours are related to Eshelby twist is considered. In a dislocation-driven growth of the nanowires, an axial screw dislocation provides the self-perpetuating steps for unidimensional growth. This mechanism, demonstrated for some semiconductor nanowires,<sup>10–13</sup> was proposed by Sears<sup>14</sup> to explain the growth of whiskers. One difficulty in assessing the existence of a dislocation related growth in thin nanowires is that dislocations are not stable in small volumes, so they can move or be worked out during handling and are not observed in TEM. However, even if a dislocation is not observed, other signs that result from screw dislocations, such as hollow tubes or Eshelby twist, can be considered.<sup>11,12</sup> According to the model of Frank,<sup>15</sup> hollow tubes, or nanopipes, can form in nanowires to reduce the elastic energy of an axial dislocation. Such nanopipes have been, for instance, observed in  $\text{In}_2\text{O}_3$  nanowires grown via evaporation-deposition.<sup>16</sup> Because the nanowires of this work do not contain nanopipes, another possible sign of strain energy created by axial dislocations would be the existence of the Eshelby twist mechanism, which can be studied through TEM imaging and diffraction techniques. In particular, the Eshelby twist in nanowires can be detected by performing twist contour analysis as originally described Drum<sup>17</sup> and as applied in Ref. 13 to the case of ZnO nanowires. The analysis enables one to determine whether the dark contours, as with those in Fig. 4(b), are the bend contours often observed in nanowires or twist contours caused by a dislocation related lattice twist along the growth axis. The amount  $\alpha$  of the Eshelby twist is<sup>18,19</sup>

$$\alpha = b/\pi r^2, \quad (1)$$

where  $b$  is the Burgers vector and  $r$  is the radius of the nanowire. In the diffraction analysis, described in detail in Refs. 13 and 17, DF images of the nanowires are recorded by using the diffracted beams corresponding to the  $+\mathbf{g}$  and  $-\mathbf{g}$  vectors orthogonal to the nanowire axis. Under these conditions, each twist contour is associated with one set of planes and is differentiated in the DF images. This is observed in the DF images of the nanowire in Figs. 4(c) and 4(d), recorded with the  $(1\bar{2}0)$  and  $(\bar{1}20)$  reflections, respectively. This observation suggests that the contours labeled  $(1\bar{2}0)$  and  $(\bar{1}20)$  in Fig. 4(a) are twist contours. The Eshelby twist between the indexed contours associated with the reciprocal vectors  $\mathbf{g}_1$  and  $\mathbf{g}_2$  is<sup>13,17</sup>

$$\alpha = (\lambda/2L)|\mathbf{g}_2 - \mathbf{g}_1|, \quad (2)$$

where  $\lambda$  is the electron wavelength and  $L$  is the distance between the indexed contours. The application of Eq. (2) to the nanowire in Fig. 4(b) yields a twist value of  $3.4^\circ/\mu\text{m}$ , which, taking into account that the angle depends on the nanowire radius, is on the order of previously reported twists in ZnO<sup>13</sup> and PbS<sup>10</sup> nanowires. For the measured  $\alpha$  value in the nanowire with a 70 nm radius, a Burgers vector of about 0.9 nm is obtained from Eq. (1). The results of the contour analysis appear then to be compatible with a dislocation-driven growth of the Fe doped ZnO nanowires.

The effect of Fe incorporation on the luminescence of the nanostructures was studied via CL in a SEM and via  $\mu$ -PL in an optical microscope. In sample A, with the lowest fraction of iron in the precursor, CL spectra show an intense defect band in the green range and a weak near bandedge emission, and the  $\text{Fe}^{3+}$  characteristic emission is not observed (Fig. 5(a)). The CL spectra of samples B and C show a 1.71 eV emission corresponding to the phonon-assisted sideband of the intraionic transition  ${}^4T_1(\text{G}) \rightarrow {}^6A_1(\text{S})$  of the  $\text{Fe}^{3+}$  ion<sup>5</sup> (Fig. 5(b)). The presence of iron in these samples also induces a shift of approximately 20 meV in the bound excitons (from 3.33 to 3.31 eV) and the donor acceptor pair (from 3.25 to 3.23 eV) luminescence, as shown in Fig. 5(c). Also, the deep level band of iron doped wires shows a redshift relative to the undoped material. A similar redshift is reported in iron doped nanostructures in Ref. 4. CL and  $\mu$ -PL images of the nanostructures show arrays of bright and dark fringes perpendicular to the growth axis (Fig. 6). CL images of the urchins or of the pseudotubular arrangements in Figs. 2(d) and 2(e) do not reveal a significant contrast. However, in Fig. 7(a) a  $\mu$ -PL image of the urchins, excited with 365 nm light, shows contrast between the ZnO defects band (green luminescence) and the  $\text{Fe}^{3+}$  phonon-assisted intraionic transitions (red luminescence). The nanorods show the same green-red contrast, and the presence of the dopant in these structures is confirmed by the  $\mu$ -PL spectrum (Fig. 7(b)), which shows  $\text{Fe}^{3+}$  zero phonon line transition at 1.79 eV,<sup>5</sup> separate from the pure ZnO defects band (2.4 eV).

We suggest that the fringe contrast in Fig. 6 is due to the inhomogeneous distribution of recombination centers, point defects, or stacking faults. This possibility agrees with the

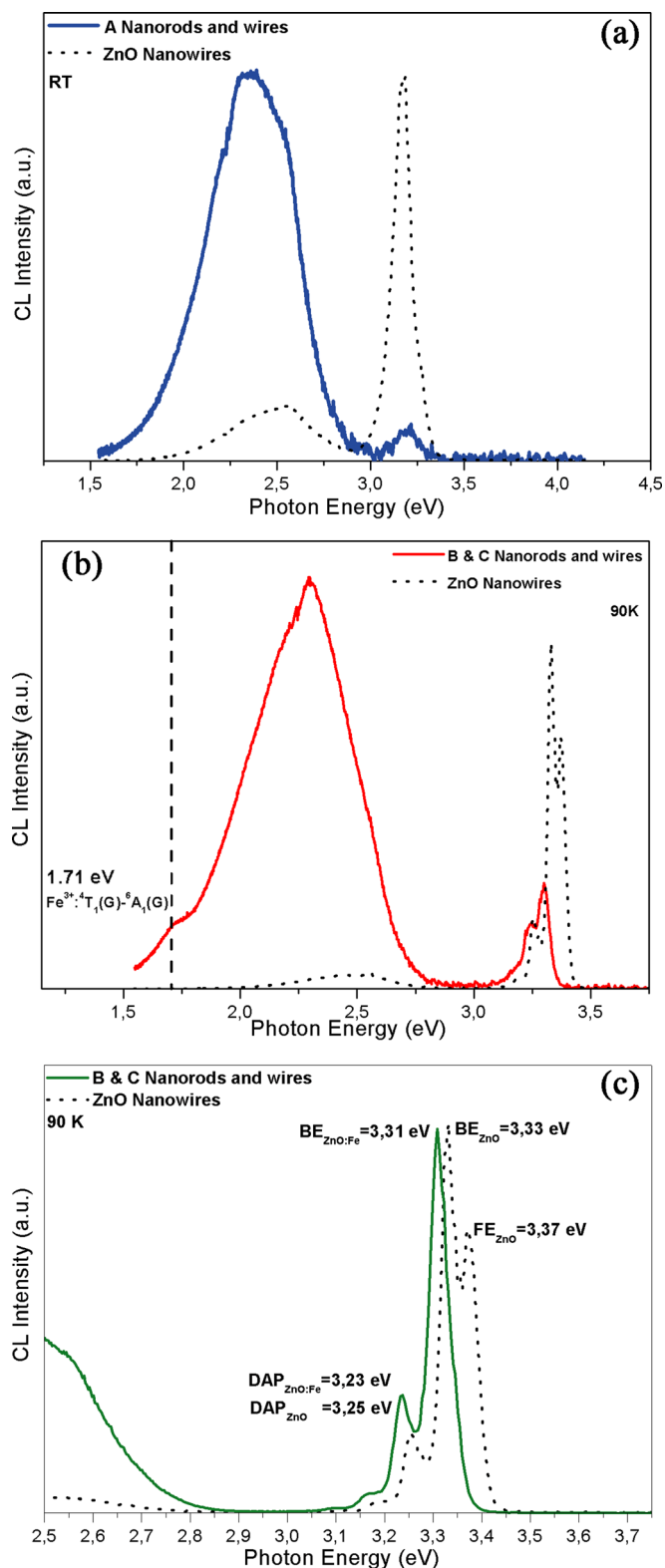


FIG. 5. (Color online) (a) CL spectra at RT recorded on nanorods and wires in sample A (solid line) compared to pure ZnO nanowires (dotted line). (b),(c) CL spectra at 90 K recorded on nanorods and wires in samples B and C (solid line) compared to pure ZnO nanowires (dotted line): (b) shows the phonon-assisted intraionic transition of  $\text{Fe}^{3+}$  (1.71 eV) and (c) shows the 20 meV redshift of the bound exciton and donor-acceptor pair luminescence.

recently reported<sup>20</sup> spatial variations of CL intensity in ZnO nanowires, which are directly related to the stacking-fault induced quenching of luminescence. The compositional

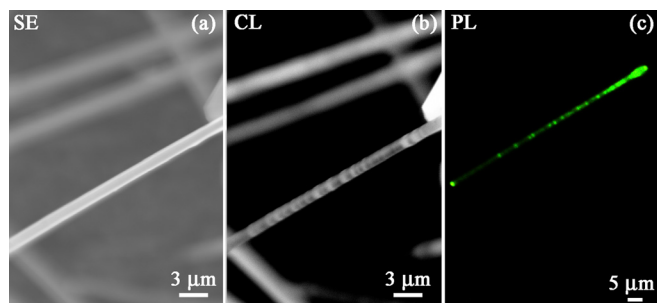


FIG. 6. (Color online) (a) Secondary electron (SE), (b) CL, and (c)  $\mu$ -PL ( $\lambda_{\text{EX}} = 365$  nm) images of a nanorod showing luminescence contrast in fringes.

measurements do not enable a determination as to whether this contrast is also related to the inhomogeneous incorporation of iron. Bright and dark rings perpendicular to the growth axis have been reported in CL images of pure ZnO (Ref. 6) and CdSe (Ref. 21) microrods. The main features of the CL and  $\mu$ -PL spectra of the Fe doped nanostructures—enhanced green band and intraionic emission—agree with the luminescence of iron implanted ZnO nanowires reported

in Ref. 5. The intense green band indicates a high concentration of defects in the nanowires, but this might depend on the growth process. Relative enhancement of the green band in Fe doped nanorods was reported in Ref. 3, whereas the opposite effect was found in Ref. 2. It is to be noted that in the mentioned luminescence works (Refs. 2 and 4), no intraionic emission of the Fe dopant was reported. It appears that the thermal growth procedure used in this work is, similar to the ion implantation in Ref. 5, effective for incorporating  $\text{Fe}^{3+}$  into the nanostructures.

#### IV. CONCLUSION

Fe doped ZnO nanowires, nanorods, and urchin-like nanostructures have been grown via an evaporation-deposition method with mixtures of ZnS and  $\text{Fe}_2\text{O}_3$  powders as precursors. The growth structures have an Fe content of about 0.5–0.7 at.%, independent of the at.% of Fe in the precursor, which agrees with the reported solubility limit of Fe in ZnO nanostructures and bulk. CL and  $\mu$ -PL show  $\text{Fe}^{3+}$  intraionic transitions at 1.71 eV and 1.79 eV, respectively, in the nanostructures and an enhanced green band relative to the undoped material. The growth axis of the nanowires as determined by HRTEM is [0001]. The results of contour analysis via transmission electron microscopy are compatible with a dislocation-driven mechanism of nanowire growth.

#### ACKNOWLEDGMENTS

This work was supported by MCINN (MAT2009-07882, CSD2009-00013) and UCM-BSCH (Group 910146).

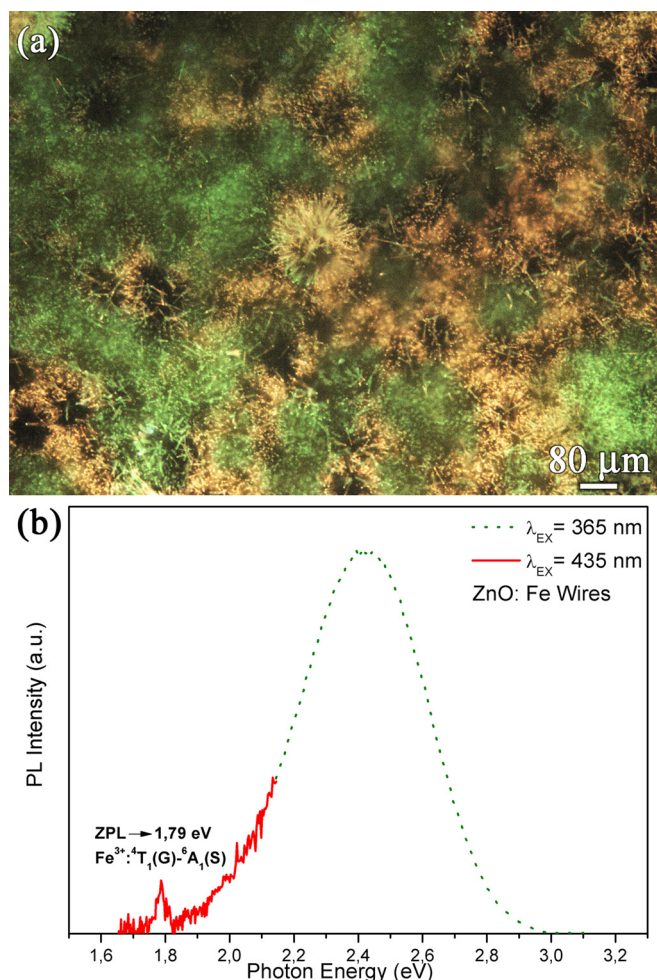


FIG. 7. (Color online) (a)  $\mu$ -PL ( $\lambda_{\text{EX}} = 365$  nm) image of the urchin-like structures of sample B, showing the luminescence contrast between the  $\text{Fe}^{3+}$  luminescence (bright areas) and the green band ZnO luminescence (dark areas). (b)  $\mu$ -PL spectrum of the nanorods ( $\lambda_{\text{EX}} = 365$  and 435 nm) showing the zero-phonon line emission of  $\text{Fe}^{3+}$  (1.79 eV).

- <sup>1</sup>C. X. Xu, X. W. Sun, Z. L. Dong, M. B. Yu, Y. Z. Xiong, and J. S. Chen, *Appl. Phys. Lett.* **86**, 173110 (2005).
- <sup>2</sup>S. Baek, J. Song, and S. Lim, *Physica B* **399**, 101 (2007).
- <sup>3</sup>E. Oh, S. H. Jung, S. H. Jeong, S. Yu, and S. J. Rhee, *Mater. Lett.* **62**, 3456 (2008).
- <sup>4</sup>B. Zhang, S. Zhou, H. Wang, and Z. Du, *Chin. Sci. Bull.* **53**, 1639 (2008).
- <sup>5</sup>S. Müller, M. Zhou, Q. Li, and C. Ronning, *Nanotechnology* **20**, 135704 (2009).
- <sup>6</sup>L. Khomenkova, P. Fernández, and J. Piqueras, *Cryst. Growth Des.* **7**, 836 (2007).
- <sup>7</sup>O. Köster-Scherger, H. Schmid, N. Vanderschaeghe, F. Wolf, and W. Mader, *J. Am. Ceram. Soc.* **90**, 3984 (2007).
- <sup>8</sup>J. Chen, J. Liu, A. West, Y. Yan, M. Yu, and W. Zhou, *IEEE Trans. Magn.* **44**, 2681 (2008).
- <sup>9</sup>Z. Jin, T. Fukumura, M. Kawasaki, K. Ando, H. Saito, T. Sekiguchi, Y. Z. Yoo, M. Murakami, Y. Matsumoto, T. Hasegawa, and H. Koinuma, *Appl. Phys. Lett.* **78**, 3824 (2001).
- <sup>10</sup>M. J. Bierman, Y. K. A. Lau, A. V. Kvit, A. L. Schmitt, and S. Jin, *Science* **320**, 1060 (2008).
- <sup>11</sup>S. A. Morin, M. J. Bierman, J. Tong, and S. Jin, *Science* **328**, 476 (2010).
- <sup>12</sup>S. Jin, M. J. Bierman, and S. A. Morin, *J. Phys. Chem. Lett.* **1**, 1472 (2010).
- <sup>13</sup>S. A. Morin and S. Jin, *Nano Lett.* **10**, 3459 (2010).
- <sup>14</sup>G. W. Sears, *Acta Metall.* **3**, 367 (1955).
- <sup>15</sup>F. C. Frank, *Acta Crystallogr.* **4**, 497 (1951).
- <sup>16</sup>D. Maestre, D. Häussler, A. Cremades, W. Jäger, and J. Piqueras, *Cryst. Growth Des.* **11**, 1117 (2011).
- <sup>17</sup>C. M. Drum, *J. Appl. Phys.* **36**, 824 (1965).
- <sup>18</sup>J. D. Eshelby, *J. Appl. Phys.* **24**, 176 (1953).
- <sup>19</sup>J. D. Eshelby, *Philos. Mag.* **3**, 440 (1958).
- <sup>20</sup>B. Sieber, A. Addad, S. Szuneris, and R. Boukherroub, *J. Phys. Chem. Lett.* **1**, 3033 (2010).
- <sup>21</sup>A. Urbieto, P. Fernández, and J. Piqueras, *Appl. Phys. Lett.* **85**, 5968 (2004).